Title	Kurtosis analysis of neural diffusion organization
Author(s)	Hui, ESK; Glenn, GR; Helpern, JA; Jensen, JH
Citation	NeuroImage, 2015, v. 106, p. 391-403
Issued Date	2015
URL	http://hdl.handle.net/10722/207233
Rights	NOTICE: this is the author's version of a work that was accepted for publication in NeuroImage. Changes resulting from the publishing process, such as peer review, editing, corrections, structural formatting, and other quality control mechanisms may not be reflected in this document. Changes may have been made to this work since it was submitted for publication. A definitive version was subsequently published in NeuroImage, 2015, v. 106, p. 391-403. DOI: 10.1016/j.neuroimage.2014.11.015

Kurtosis Analysis of Neural Diffusion Organization

Edward S. Hui[a], G. Russell Glenn[b,c], Joseph A. Helpern[b,c,d], Jens H. Jensen[b,d,*]

[a]Department of Diagnostic Radiology, The University of Hong Kong, Pokfulam, Hong Kong

[b]Center for Biomedical Imaging, Medical University of South Carolina, Charleston, SC, USA

[c]Department of Neurosciences, Medical University of South Carolina, Charleston, SC, USA

[d]Department of Radiology and Radiological Science, Medical University of South Carolina, Charleston, SC, USA

*Corresponding author at: Center for Biomedical Imaging, Department of Radiology and Radiological Science, Medical University of South Carolina, 96 Jonathan Lucas, MSC 323, Charleston, SC 29425-0323, USA

E-mail address: jense@musc.edu (J. Jensen).

E-mail address: edward.s.hui@gmail.com (E. Hui).

E-mail address: glenng@musc.edu (G. Glenn).

E-mail address: helpern@musc.edu (J. Helpern).

Telephone: (843)876-2467 (J. Jensen).

ABSTRACT

A computational framework is presented for relating the kurtosis tensor for water diffusion in brain to tissue models of brain microstructure. The tissue models are assumed to be comprised of non-exchanging compartments that may be associated with various microstructural spaces separated by cell membranes. Within each compartment the water diffusion is regarded as Gaussian, although the diffusion for the full system would typically be non-Gaussian. The model parameters are determined so as to minimize the Frobenius norm of the difference between the measured kurtosis tensor and the model kurtosis tensor. This framework, referred to as kurtosis analysis of neural diffusion organization (KANDO), may be used to help provide a biophysical interpretation to the information provided by the kurtosis tensor. In addition, KANDO combined with diffusional kurtosis imaging can furnish a practical approach for developing candidate biomarkers for neuropathologies that involve alterations in tissue microstructure. KANDO is illustrated for simple tissue models of white and gray matter using data obtained from healthy human subjects.

Keywords: Kurtosis, Diffusion, Microstructure, Tissue Model, MRI

Introduction

Non-Gaussianity of water diffusion within the brain can be quantified by the diffusional kurtosis tensor, which may be measured with MRI using diffusional kurtosis imaging (DKI) (Hori et al., 2012; Jensen and Helpern, 2010; Jensen et al., 2005; Lu et al., 2006; Poot et al., 2010; Steven et al., 2014; Wu and Cheung, 2010). This kurtosis tensor allows a number of rotationally invariant diffusion metrics to be calculated, including the mean kurtosis (MK), the axial kurtosis, and the radial kurtosis. These metrics are believed to reflect the heterogeneity of the intra-voxel diffusion environment and are thus indicators of microstructural complexity. A number of studies have shown that kurtosis-based diffusion metrics are altered for a variety of neuropathologies, such as stroke (Cheung et al., 2012; Hui et al., 2012; Jensen et al., 2011), cancer (Raab et al., 2010; Van Cauter et al., 2012), Alzheimer's disease (Benitez et al., 2014; Falangola et al., 2013; Fieremans et al., 2013; Gong et al., 2013), epilepsy (Gao et al., 2012; Lee et al., 2013; Lee et al., 2014; Zhang et al., 2013), Parkinson's disease (Kamagata et al., 2014; Kamagata et al., 2013), attention deficit hyperactivity disorder (Adisetiyo et al., 2014; Helpern et al., 2011), trauma (Grossman et al., 2012; Grossman et al., 2013; Zhuo et al., 2012), and autism (Lazar et al., 2014).

Since the kurtosis tensor is a pure diffusion measure, without any explicit connections to specific properties of brain tissue microstructure, a clear-cut biophysical interpretation of the information it provides for a particular circumstance (e.g., brain region or disease) is often challenging (Rudrapatna et al., 2014). It may therefore be useful to combine the kurtosis tensor with tissue models that relate the diffusion information of the kurtosis tensor to particular microstructural features of cellular compartments. With the help of such models, the biological significance of observed changes in kurtosis can be better understood. In addition, the model

parameters may serve as candidate biomarkers for microstructural alterations associated with disease.

One such tissue model for the kurtosis tensor has been previously proposed, although its applicability is limited to white matter for which the axons are largely unidirectional (Fieremans et al., 2011). An example of the relationships implied by this model is the formula

$$f_{axon} = \frac{K_{\max}}{K_{\max} + 3}, \tag{1}$$

where f_{axon} is the fraction of MRI-visible water contained within axons and $K_{\max}$ is the maximum value of the diffusional kurtosis as a function of the diffusion direction. This model has already been applied to Alzheimer's disease (Benitez et al., 2014; Fieremans et al., 2013), stroke (Hui et al., 2012), and autism (Lazar et al., 2014).

The purpose of this study is to develop a more general computational framework for relating the kurtosis tensor to tissue models of brain microstructure. This method, which we call kurtosis analysis of neural diffusion organization (KANDO), accommodates a variety of models that are suitable for both white matter and gray matter. The models are assumed to consist of ensembles of non-exchanging, Gaussian compartments. This is a plausible class of models that has been widely used to describe non-Gaussian diffusion in brain (Alexander et al., 2002; Assaf et al., 2004; Fieremans et al., 2011; Jespersen et al., 2007; Panagiotaki et al., 2009; Panagiotaki et al., 2012; Wang et al., 2011; White et al., 2013; Zhang et al., 2012). While the effects of water exchange between compartments are not incorporated explicitly, their consideration is important for a proper interpretation of these models.

The essence of KANDO is that the model parameters are determined by minimizing a cost function that corresponds to the square of the Frobenius norm (Signoretto et al., 2011) of the

difference between the measured kurtosis tensor and the model kurtosis tensor. This contrasts with the algebraic approach utilized by Fieremans and coworkers (Fieremans et al., 2011) in that KANDO requires nonlinear optimization. However, KANDO provides substantially more flexibility than is possible with purely algebraic methods, allowing for a much broader range of model types. Moreover, one can easily construct specific models for KANDO that yield results closely matching those of Fieremans and coworkers for white matter with unidirectional axons. In this sense, KANDO may be regarded as an extension of this prior work.

KANDO is quite analogous to the conventional method of fitting tissue models to the diffusion MRI (dMRI) signal (Assaf et al., 2004; Ferizi et al., 2013; Jespersen et al., 2007; Panagiotaki et al., 2009; Panagiotaki et al., 2012; Wang et al., 2011; White et al., 2013; Zhang et al., 2012) with a key difference being that KANDO utilizes only the kurtosis and diffusion tensors as inputs, rather than the full dMRI signal, in order to facilitate a clearer biophysical interpretation of the kurtosis tensor information. KANDO is particularly suitable as an adjunct for DKI, which is specifically designed for estimating the kurtosis and diffusion tensors. One distinction between KANDO and tissue modeling based on fits to the dMRI signal is that KANDO does not require the specification of imaging parameters, such as diffusion gradient directions and b-values, which may help to reduce the dependence on experimental details of results obtained with KANDO. Nonetheless, KANDO estimates for model parameters may be indirectly affected by imaging parameters, as these can influence the accuracy of the measured diffusion and kurtosis tensors (Jensen and Helpern, 2010). As KANDO only includes information encompassed by the kurtosis and diffusion tensors, it may be insensitive to certain microstructural features that affect the full signal.

The main goal of this article is to describe the general theory underlying KANDO. In addition, KANDO is illustrated for three simple models intended to represent white matter and gray matter. For these models, exemplary results are given based on DKI data obtained for healthy human volunteers. In addition, numerical simulations are described that examine potential sources of errors in parameter estimates obtained with KANDO.

Theory

General framework

A fundamental assumption of KANDO is that the tissue model consists of $N+1$ non-exchanging water compartments. Each individual compartment is also assumed have Gaussian diffusion with its dynamics being completely determined by its diffusion tensor. Let the diffusion tensor for the *n*th compartment be indicated by $\mathbf{D}^{(n)}$ and the corresponding water fraction by f_n. Here the water fractions are relative only to water that is visible with dMRI. Thus some water pools with short T2, such as water within myelin (Stanisz et al., 1999), might be excluded from the model, depending on the echo time of the dMRI experiment. It should be noted that the total diffusion dynamics of a model with two or more Gaussian compartments will generally be non-Gaussian, as the sum of two or more Gaussian distributions is a non-Gaussian distribution except for the special case that all the distributions are identical.

It is physically appealing to associate the model compartments with cellular compartments of the tissue microstructure, and this is generally justified for cells with low permeability plasma membranes. For example, water within myelinated axons has an exchange time with the surrounding extracellular space that is long compared to typical diffusion times used for dMRI (Nilsson et al., 2013), and thus this compartment can plausibly be approximated as non-exchanging. However, other cell types, such as astrocytes, may have substantially shorter

exchange times (Badaut et al., 2011; Solenov et al., 2004). When the exchange time is small compared to the diffusion time, a cellular compartment can be regarded as being in fast exchange with the extracellular space, and it is then effectively part of a larger composite compartment that includes the extracellular space and possibly other cellular compartments also in fast exchange. As there is currently limited knowledge of the exchange times for glial cells and unmyelinated neurites, the precise correspondence between model and cellular compartments may not always be self-evident. When the exchange and diffusion times are comparable, the model compartments can take on a more ambiguous "apparent" status.

The total diffusion tensor for the model is

$$\mathbf{D} = \sum_{n=0}^{N} f_n \mathbf{D}^{(n)} , \tag{2}$$

where the $N+1$ compartments are numbered from $n=0$ to $n=N$ and with the water fractions being normalized so that

$$1 = \sum_{n=0}^{N} f_n . \tag{3}$$

$\mathbf{D}$ is regarded as a measured quantity that is a fixed input from a modeling perspective. It is convenient to introduce the "reduced" diffusion tensors defined by

$$\mathbf{\Delta} \equiv \frac{\mathbf{D}}{\overline{D}} \qquad \text{and} \qquad \mathbf{\Delta}^{(n)} \equiv \frac{\mathbf{D}^{(n)}}{\overline{D}} , \tag{4}$$

where $\overline{D} = Tr(\mathbf{D})/3$ is the mean diffusivity for the total system. These reduced tensors are dimensionless and serve to simplify the mathematical expressions that follow. In terms of the reduced tensors, Eq. (2) takes the form

$$\boldsymbol{\Delta} = \sum_{n=0}^{N} f_n \boldsymbol{\Delta}^{(n)} . \tag{5}$$

Since $\boldsymbol{\Delta}$ depends only on $\mathbf{D}$, it is also a given input for KANDO.

Let us now assume that the reduced diffusion tensors for compartments $n = 1,2,\ldots,N$, as well as their corresponding water fractions, are specified functions of a set of M model parameters $(a_1, a_2, \ldots, a_M)$ so that we have $\boldsymbol{\Delta}^{(n)}(a_m)$ and $f_n(a_m)$, for $n = 1,2,\ldots,N$. These functions would be based on the biophysical assumptions for the water diffusion dynamics in brain tissue that one wishes to employ. By applying Eqs. (3) and (5), we also have

$$f_0(a_m) = 1 - \sum_{n=1}^{N} f_n(a_m), \tag{6}$$

and

$$\boldsymbol{\Delta}^{(0)}(a_m) = \frac{\boldsymbol{\Delta} - \sum_{n=1}^{N} f_n(a_m)\boldsymbol{\Delta}^{(n)}(a_m)}{1 - \sum_{n=1}^{N} f_n(a_m)}, \tag{7}$$

which determines f_0 and $\boldsymbol{\Delta}^{(0)}$ in terms of the model parameters.

Here the compartment for $n = 0$ plays a special role in that its properties are inferred from Eqs. (6) and (7) rather than being modeled directly. This "slack" compartment should be chosen so that its water fraction f_0 is unlikely to vanish, as that would lead to singularities in the KANDO optimization procedure described below. In addition, it may be convenient for the slack compartment to represent a component of brain tissue that is less amenable to detailed modeling (e.g., the extracellular space).

As for $\mathbf{D}$ and $\mathbf{\Delta}$, the measured kurtosis tensor for the total system, $\mathbf{W}$, is considered to be a known quantity, as determined for example with DKI. On the other hand, the total kurtosis tensor for the model, $\mathbf{W}^{\mathrm{mod}}$, is related to the reduced diffusion tensors by (Lazar et al., 2008)

$$W_{ijkl}^{\mathrm{mod}}(a_m) = \sum_{n=0}^{N} f_n(a_m)\left[\Delta_{ij}^{(n)}(a_m)\Delta_{kl}^{(n)}(a_m) + \Delta_{ik}^{(n)}(a_m)\Delta_{jl}^{(n)}(a_m) + \Delta_{il}^{(n)}(a_m)\Delta_{jk}^{(n)}(a_m)\right] - \left(\Delta_{ij}\Delta_{kl} + \Delta_{ik}\Delta_{jl} + \Delta_{il}\Delta_{jk}\right), \tag{8}$$

with Δ_{ij}, $\Delta_{ij}^{(n)}$, and W_{ijkl}^{mod} representing the components of $\mathbf{\Delta}$, $\mathbf{\Delta}^{(n)}$, and $\mathbf{W}^{\mathrm{mod}}$, respectively. The component indices for all the tensors run from 1 to 3. $\mathbf{W}^{\mathrm{mod}}$ is therefore a specified function of the model parameters a_m.

The basic computational problem of KANDO is to optimize the model parameters a_m in order to minimize the cost function

$$C \equiv \sum_{i,j,k,l=1}^{3} \left| W_{ijkl}^{\mathrm{mod}}(a_m) - W_{ijkl} \right|^2 \tag{9}$$

so that the model and measured kurtosis tensors are as "close" as possible. This cost function simply corresponds to the square of the Frobenius norm of the difference between the predicted and measured kurtosis tensors. The Frobenius norm is the natural extension to tensors of the familiar l_2 vector norm (Signoretto et al., 2011).

Since the kurtosis tensor has 15 independent degrees of freedom, the number of model parameters should, in principle, be chosen to be no more than this. In practice, the number of model parameters would usually be substantially less. In most cases, minimization of C corresponds to a nonlinear optimization problem. If the number of model parameters is modest, such problems can often be conveniently solved using standard numerical algorithms, although computational challenges such as multiple local minima may well occur. For the special case of

completely isotropic tissue, the kurtosis tensor has only a single independent degree of freedom, and KANDO therefore can only support a single model parameter. The same can also hold true for nearly isotropic tissue, such as gray matter, as the observed anisotropy may largely reflect the effects of signal noise.

In order that the model parameters correspond to physically meaningful diffusion dynamics, the minimization of C would usually be subject to constraints that ensure the reduced diffusion tensors $\mathbf{\Lambda}^{(n)}$ are semi-positive definite and that the water fractions lie in the range $0 \leq f_n \leq 1$. Imposing additional conditions, such as maximum values for diffusivities, may also be of value.

Because Eq. (5) is used in the construction of the function $W_{ijkl}^{\mathrm{mod}}(a_m)$, the total diffusion tensor for the model will always be exactly equal to the measured diffusion tensor. The model prediction for the kurtosis tensor, however, will differ from the measured kurtosis tensor, except for the exceptional circumstance that the cost function can be reduced to zero.

From minimizing C, one obtains estimates for the model parameters a_m, which by design should reflect certain microstructural tissue properties. In addition, KANDO yields estimates for the volume fractions of all the compartments, as well as their individual diffusion tensors. In this way, the microstructural organization of the diffusion dynamics is characterized. For well-conceived models, there should typically be a unique global minimum for C that yields a unique set of model parameters.

In the above, we have used a finite number of compartments denoted with the discrete index n. However, it is straightforward to generalize this KANDO formalism to include an

infinite number of compartments denoted with a continuous index. This is useful, for example, in modeling neurites with a continuous distribution of orientations.

Example 1: white matter with unidirectional axons

As a first example of KANDO, we consider a model for white matter with unidirectional axons, as illustrated in the first panel of Fig. 1. The physical assumptions underlying this model are essentially the same as those for the algebraic approach considered by Fieremans and coworkers (Fieremans et al., 2011) , who have provided a detailed discussion of their validity.

Since two compartments are considered, we have $N=1$. The slack compartment is taken to represent both water in the extracellular space and water in glial cells, which are treated as a single composite compartment, and the $n=1$ compartment is taken to represent water within axons. Water within myelin is assumed to not contribute significantly to the dMRI signal and is therefore neglected.

The intra-axonal water for the $n=1$ compartment is regarded as being confined to thin cylinders oriented parallel to the principal eigenvector, $\mathbf{e}$, of the total diffusion tensor $\mathbf{D}$. This principal eigenvector, corresponding to the largest eigenvalue of $\mathbf{D}$, is normalized so that $|\mathbf{e}|=1$. Because of the thin cylinder approximation, the reduced diffusion tensor components for the $n=1$ compartment can be written as

$$\Delta_{ij}^{(1)}(a_m) = a_1 e_i e_j , \tag{10}$$

where e_i is a component of $\mathbf{e}$. The intra-axonal diffusivity then vanishes for directions perpendicular to $\mathbf{e}$, and the intrinsic intra-axonal diffusivity (i.e., the diffusivity along the cylinder axis) is $\overline{D}a_1 \equiv D^*$.

As discussed in the Appendix, the axonal water fraction for this model may be estimated, depending on which assumptions are made, from the total kurtosis maximized over either all diffusion directions or over just diffusion directions that are perpendicular to $\mathbf{e}$, as indicated by Eqs. (A.22) and (A.23). Thus we set

$$f_1 = f_{axon} = \frac{K_{\max}}{K_{\max}+3} \quad \text{or} \quad \frac{K_{\perp,\max}}{K_{\perp,\max}+3}, \tag{11}$$

with $K_{\max}$ being the global maximum for the total kurtosis and with $K_{\perp,\max}$ being the maximum over directions perpendicular to $\mathbf{e}$. The option using $K_{\max}$ may at times be the more accurate estimate, as it represents the true global maximum, but the option using $K_{\perp,\max}$ is based on milder assumptions and is therefore potentially more foolproof (see last sentence of Appendix). While prior work has only utilized the $K_{\max}$ option (Benitez et al., 2014; Fieremans et al., 2013; Fieremans et al., 2011; Gong et al., 2014; Hui et al., 2012; Lazar et al., 2014), we consider both in this study. Since $K_{\max}$ and $K_{\perp,\max}$ are determined by $\mathbf{D}$ and $\mathbf{W}$, these are known quantities, as then is f_1. As a consequence, this model has a single free model parameter, a_1, so that $M = 1$.

From Eqs. (6) and (11), we have

$$f_0 = 1 - f_1 = \frac{3}{K_{\max}+3} \quad \text{or} \quad \frac{3}{K_{\perp,\max}+3}, \tag{12}$$

implying that f_0 is also independent of a_1, and from Eq. (7) we have

$$\mathbf{\Delta}^{(0)}(a_m) = \frac{1}{f_0}\left[\mathbf{\Delta} - f_1\mathbf{\Delta}^{(1)}(a_m)\right]. \tag{13}$$

Combining Eqs. (8), (10) and (13) then yields

$$W_{ijkl}^{\mathrm{mod}}(a_m) = 3 f_1 a_1^2 e_i e_j e_k e_l - \Delta_{ij}\Delta_{kl} - \Delta_{ik}\Delta_{jl} - \Delta_{il}\Delta_{jk} + \frac{1}{f_0}\left[\left(\Delta_{ij} - f_1 a_1 e_i e_j\right)\left(\Delta_{kl} - f_1 a_1 e_k e_l\right)\right.$$
$$\left. + \left(\Delta_{ik} - f_1 a_1 e_i e_k\right)\left(\Delta_{jl} - f_1 a_1 e_j e_l\right) + \left(\Delta_{il} - f_1 a_1 e_i e_l\right)\left(\Delta_{jk} - f_1 a_1 e_j e_k\right)\right]. \quad (14)$$

Thus $\mathbf{W}^{\mathrm{mod}}$ depends quadratically on a_1, and as then follows from Eq. (9), the cost function C is a quartic polynomial in a_1. Note that a_1 is the only degree of freedom for $\mathbf{W}^{\mathrm{mod}}$, with the other parameters in Eq. (14) being fixed by the measured diffusion and kurtosis tensors. In order to ensure that the reduced diffusion tensors for the two compartments are both semi-positive definite, the minimization of C should be carried out subject to the constraint

$$0 \le a_1 \le \frac{\lambda_1}{\overline{D} f_1}, \quad (15)$$

where λ_1 is the largest eigenvalue of $\mathbf{D}$.

An additional optional constraint is requiring the intrinsic intra-axonal diffusivity to be less than or equal to a set maximum value, $D_{\max}^*$, which can be expressed as

$$a_1 \le \frac{D_{\max}^*}{\overline{D}}. \quad (16)$$

For example, one could choose $D_{\max}^* = 3.0\,\mu\mathrm{m}^2/\mathrm{ms}$ so as to be equal the free diffusivity of water at body temperature (Holz et al., 2000). This extra condition may be helpful in reducing outliers arising from noise, imaging artifacts, and partial volume effects.

Example 2: white matter with crossing fibers

In white matter regions with crossing fibers, a single direction is inadequate to characterize the axonal geometry. By calculating the diffusion orientation distribution function (dODF), multiple fiber directions can be detected using dMRI, with the fiber directions corresponding to the dODF maxima (Lazar et al., 2008; Tuch, 2004; Wedeen et al., 2005).

Recently, an approximate analytical expression for the dODF in terms of the kurtosis and diffusion tensors has been derived (Jensen et al., 2014a). Fiber directions obtained with this "kurtosis dODF" may thus be incorporated into KANDO for the modeling of white matter with fiber crossings.

Here we consider the case where two fiber bundles intersect within a given voxel (see Fig. 1, second panel). Assume that the fiber directions are given by the vectors $\mathbf{v}^{(1)}$ and $\mathbf{v}^{(2)}$. As these can be determined from $\mathbf{D}$ and $\mathbf{W}$, via the kurtosis dODF, $\mathbf{v}^{(1)}$ and $\mathbf{v}^{(2)}$ may be treated as fixed inputs for KANDO. The KANDO compartments are then the extra-axonal space (slack), axons oriented in the direction $\mathbf{v}^{(1)}$ ($n=1$) and axons oriented in the direction $\mathbf{v}^{(2)}$ ($n=2$), and so we have $N=2$. Myelin water is neglected, as for Example 1. The magnitudes of both direction vectors are normalized to unity. We assume that the direction $\mathbf{v}^{(1)}$ corresponds to the larger of the dODF maxima and hence to the dominant fiber direction. Since the kurtosis dODF typically detects relatively few voxels with more than two intra-voxel fiber directions (Jensen et al., 2014a), this example is potentially applicable to many white matter regions. This is assuming, of course, that the kurtosis dODF provides an adequate description of the fiber architecture.

Again using the thin cylinder approximation, the components of the reduced diffusion tensors for compartments 1 and 2, are given by

$$\Delta_{ij}^{(1)}(a_m) = a_1 \mathrm{v}_i^{(1)} \mathrm{v}_j^{(1)} \tag{17}$$

and

$$\Delta_{ij}^{(2)}(a_m) = a_1 \mathrm{v}_i^{(2)} \mathrm{v}_j^{(2)}, \tag{18}$$

where $\mathrm{v}_i^{(1)}$ indicates a component of $\mathbf{v}^{(1)}$ and $\mathrm{v}_i^{(2)}$ indicates a component of $\mathbf{v}^{(2)}$. The intrinsic intra-axonal diffusivity is then $D^* = \overline{D}a_1$ for both compartments.

The total axonal water fraction, $f_1 + f_2$, is determined by the total kurtosis, $K_\perp$, in a direction orthogonal to both $\mathbf{v}^{(1)}$ and $\mathbf{v}^{(2)}$, as discussed in the Appendix. Specifically,

$$f_{axon} = f_1 + f_2 = \frac{K_\perp}{K_\perp + 3}. \tag{19}$$

as follows from Eq. (A.15). We can then choose

$$f_1(a_m) = a_2, \tag{20}$$

which together with Eq. (19) implies that

$$f_2(a_m) = \frac{K_\perp}{K_\perp + 3} - a_2 \tag{21}$$

and that $M = 2$. The water fraction for the slack compartment must be

$$f_0 = 1 - f_1 - f_2 = \frac{3}{K_\perp + 3}, \tag{22}$$

which is a fixed parameter, and the reduced diffusion tensor for the slack compartment is

$$\mathbf{\Delta}^{(0)}(a_m) = \frac{1}{f_0}\left[\mathbf{\Delta} - f_1(a_m)\mathbf{\Delta}^{(1)}(a_m) - f_2(a_m)\mathbf{\Delta}^{(2)}(a_m)\right], \tag{23}$$

as follows from Eq. (7).

With these results and the help of Eq. (8), $\mathbf{W}^{\mathrm{mod}}(a_m)$ for this model is readily constructed, and its components are seen to be multivariate polynomials of degrees up to 4. This implies that the cost function C is a multivariate polynomial of degree 8.

In minimizing C, one should impose constraints to guarantee that the parameters a_1 and a_2 are in physically allowed ranges. To specify these conditions, it is convenient to introduce the pair of vectors

$$\mathbf{v}^{(\pm)} \equiv \frac{\mathbf{v}^{(1)} \pm \mathbf{v}^{(2)}}{\sqrt{4\alpha_{\pm}}}, \tag{24}$$

where

$$\alpha_{\pm} \equiv \frac{1}{2}\left[1 \pm \mathbf{v}^{(1)} \cdot \mathbf{v}^{(2)}\right]. \tag{25}$$

One may easily verify that $\left|\mathbf{v}^{(\pm)}\right| = 1$ and $\mathbf{v}^{(+)} \cdot \mathbf{v}^{(-)} = 0$. Therefore, $\mathbf{v}^{(+)}$ and $\mathbf{v}^{(-)}$ constitute a set of orthonormal basis vectors that span the plane containing $\mathbf{v}^{(1)}$ and $\mathbf{v}^{(2)}$. Let us also define

$$\Delta_{++} \equiv \left[\mathbf{v}^{(+)}\right]^T \mathbf{\Delta} \mathbf{v}^{(+)}, \qquad \Delta_{--} \equiv \left[\mathbf{v}^{(-)}\right]^T \mathbf{\Delta} \mathbf{v}^{(-)}, \text{ and } \qquad \Delta_{+-} \equiv \left[\mathbf{v}^{(+)}\right]^T \mathbf{\Delta} \mathbf{v}^{(-)}. \tag{26}$$

The required constraints on a_1 and a_2 can then be written as

$$0 \le a_1 \le \frac{\Delta_{++} + \Delta_{--}}{1 - f_0}, \tag{27}$$

$$\frac{1 - f_0}{2} \le a_2 \le 1 - f_0 \tag{28}$$

and

$$\left[\Delta_{+-} + a_1(1 - f_0 - 2a_2)\sqrt{\alpha_+ \alpha_-}\right]^2 \le \left[\Delta_{++} - a_1\alpha_+(1 - f_0)\right] \cdot \left[\Delta_{--} - a_1\alpha_-(1 - f_0)\right]. \tag{29}$$

The lower bound of Eq. (28) is based on the assumption that $\mathbf{v}^{(1)}$ is the dominant fiber direction. The final condition of Eq. (29) is needed to ensure that $\mathbf{\Delta}^{(0)}$ is semi-positive definite. The constraint of Eq. (16) may be additionally imposed to further restrict the allowed values of a_1.

This model is also suitable for voxels with a single fiber direction, as this corresponds to the special case for which $f_2 = 0$. However in such cases, $K_\perp$ is not well defined, and so in Eq. (19), we use the maximum kurtosis sampled over all directions perpendicular to $\mathbf{v}^{(1)}$ for estimating the axonal water fraction, rather than $K_\perp$.

Example 3: gray matter

For gray matter, we model the intra-neurite space (i.e., both axons and dendrites) with isotropically oriented thin cylinders (see Fig. 1, third panel). We thus have

$$\Delta_{ij}^{(\theta,\phi)}(a_m) = \frac{D^*}{\overline{D}} u_i(\theta,\phi) u_j(\theta,\phi), \tag{30}$$

with $u_i(\theta,\phi)$ being a component of the direction vector

$$\mathbf{u}(\theta,\phi) = \hat{\mathbf{x}}\sin(\theta)\cos(\phi) + \hat{\mathbf{y}}\sin(\theta)\sin(\phi) + \hat{\mathbf{z}}\cos(\theta). \tag{31}$$

Here (θ,ϕ) are spherical coordinates and $(\hat{\mathbf{x}},\hat{\mathbf{y}},\hat{\mathbf{z}})$ represent Cartesian unit vectors. In contrast to the previous two examples, the intrinsic intra-neurite diffusivity D^* is taken as a given. This is because, as previously noted, KANDO only supports a single model parameter for isotropic geometries and because f_0 cannot be determined directly from the measured kurtosis tensor as there is no direction perpendicular to all of the neurites. In Eq. (30), the discrete index n has been replaced with the continuous variables (θ,ϕ) in order to allow for a continuous angular distribution of orientations. Thus the intra-neurite space formally consists of an infinite number of Gaussian compartments.

For the neurite water fraction in a specified direction, we choose

$$f_{\theta,\phi}(a_m) = \frac{a_1}{4\pi} \tag{32}$$

so that all directions have equal weight as appropriate for an isotropic tissue. For the slack compartment, Eq. (6) then yields

$$f_0(a_m) = 1 - a_1, \tag{33}$$

and Eq. (7) yields

$$\Delta_{ij}^{(0)}(a_m) = \frac{1}{1-a_1}\left(\Delta_{ij} - \frac{a_1 D^*}{3\overline{D}}\delta_{ij}\right), \tag{34}$$

where δ_{ij} is the Kronecker delta. In deriving Eqs. (33) and (34), the sums over the index n have been replaced with an angular integration over the spherical coordinates (θ,ϕ).

By combining with Eqs. (33) and (34) with Eq. (8), we then obtain

$$\begin{aligned} W_{ijkl}^{\mathrm{mod}}(a_m) = {} & \frac{a_1 (D^*)^2}{5\overline{D}^2}\left(\delta_{ij}\delta_{kl} + \delta_{ik}\delta_{jl} + \delta_{il}\delta_{jk}\right) - \Delta_{ij}\Delta_{kl} - \Delta_{ik}\Delta_{jl} - \Delta_{il}\Delta_{jk} \\ & + \frac{1}{1-a_1}\left[\left(\Delta_{ij} - \frac{a_1 D^*}{3\overline{D}}\delta_{ij}\right)\left(\Delta_{kl} - \frac{a_1 D^*}{3\overline{D}}\delta_{kl}\right)\right. \\ & \left. + \left(\Delta_{ik} - \frac{a_1 D^*}{3\overline{D}}\delta_{ik}\right)\left(\Delta_{jl} - \frac{a_1 D^*}{3\overline{D}}\delta_{jl}\right) + \left(\Delta_{il} - \frac{a_1 D^*}{3\overline{D}}\delta_{il}\right)\left(\Delta_{jk} - \frac{a_1 D^*}{3\overline{D}}\delta_{jk}\right)\right]. \end{aligned} \tag{35}$$

The KANDO optimization for this case will thus be the minimization of a rational function in the single parameter a_1. To guarantee a physical solution, we must impose the constraints

$$0 \le a_1 < 1 \tag{36}$$

and

$$a_1 \le \frac{3\lambda_3}{D^*}, \tag{37}$$

where λ_3 is the smallest eigenvalue of $\mathbf{D}$.

Methods

Subjects

For demonstrating KANDO, two healthy volunteers (male, 26 and 52 years old) were recruited. These subjects were scanned with informed consent approved by the Institutional Review Board of the Medical University of South Carolina.

Magnetic resonance imaging

Both volunteers were scanned on a 3T Siemens TIM Trio MRI scanner (Siemens Healthcare, Erlangen, Germany) with a 32-channel transmit/receive head coil. Two sets of dMRI experiments were performed with 64 diffusion encoding directions using a vendor-supplied, single-shot, twice-refocused, spin-echo echo planar imaging sequence. Axial diffusion-weighted images (DWIs) were acquired with 3 b-values (0, 1000 and 2000 s/mm^2) and number of excitations (NEX) = 1 (NEX = 10 for b = 0). Other imaging parameters were: slice thickness = 2.7 mm (0 mm gap), number of slices = 40, repetition time/echo time = 5500/102 ms, field-of-view = 222 × 222 mm^2, acquisition matrix = 82 × 82, image resolution = 2.7 × 2.7 mm^2, bandwidth/pixel = 1355 Hz, parallel imaging acceleration factor = 2 (phase encoding), and acquisition time ≈ 14 minutes. This corresponds to a standard DKI protocol (Jensen and Helpern, 2010).

Data processing

Diffusion and diffusional kurtosis tensors were calculated for each subject with the in-house software Diffusional Kurtosis Estimator (Tabesh, 2012; Tabesh et al., 2011) on a voxel-by-voxel basis by using the full set DWIs. Parametric maps for $\overline{D}$, axial diffusivity $\lambda_{\parallel}$, radial diffusivity $\lambda_{\perp}$, fractional anisotropy (FA), and MK were subsequently obtained from these tensors.

All KANDO optimizations were performed on a voxel-by-voxel basis using MATLAB (Mathworks, Natick, MA, USA) for each of the three examples described above. In order to ensure that a global optimum was found, an exhaustive search strategy over the physically viable parameter space (as defined by the constraints) was employed for minimization of the cost function C. For Examples 1 and 3, C was evaluated for 1000 parameter space points/voxel, while for Example 2, 10,000 points/voxel were used. To process the full dataset for one subject (i.e., 82×82×40 voxels) required about 500 s for Example 1, 7700 s for Example 2, and 400 s for Example 3, using a quad core, 2.2 GHz computer with 16 GB RAM. Example 2 was more computationally intensive due to the greater number of free parameters.

For Example 2, the kurtosis dODFs were evaluated with a radial weighting factor of 4 (Jensen et al., 2014a). In voxels for which the dODF detected two or more fiber directions, the two directions corresponding to the largest dODF maxima were selected. In voxels for which the dODF detected a single direction, f_2 was set to zero, and to estimate f_0, $K_\perp$ in Eq. (22) was replaced with the maximum kurtosis optimized over directions perpendicular to $\mathbf{v}^{(1)}$. For both Examples 1 and 2, the additional constraint of Eq. (16) was imposed with $D^*_{\max} = 3.0\,\mu\text{m}^2/\text{ms}$ in order to reduce outliers due to noise, imaging artifacts, and partial volume effects. For Example 3, the intrinsic intra-neurite diffusivity was set to $D^* = 1.0\ \mu\text{m}^2/\text{ms}$, as this was considered to be a plausible value based on prior work (Fieremans et al., 2011).

Region-of-interest analysis

Three multi-slice region-of-interests (ROIs) were identified to represent presumptive white matter with unidirectional axonal fiber bundles (ROI 1), white matter (ROI 2), and gray matter (ROI 3). ROI 1 was defined by $\overline{D} < 1.5\ \mu\text{m}^2/\text{ms}$, $\text{FA} > 0.15$, $\text{MK} \geq 1.0$ and $\lambda_\parallel \geq 3\lambda_\perp$;

ROI 2 was defined by $\overline{D} < 1.5$ μm^2/ms, $\mathrm{FA} > 0.15$ and $\mathrm{MK} \geq 1.0$; ROI 3 was defined by $\overline{D} < 1.5$ μm^2/ms, $\mathrm{FA} \leq 0.15$ and $\mathrm{MK} < 1.0$. Note that ROI 1 is a subset of ROI 2. ROI 1 was used for the analysis of Example 1, ROIs 1 and 2 were used for the analysis of Example 2, and ROI 3 was used for the analysis of Example 3. The restriction $\overline{D} < 1.5$ μm^2/ms was imposed to exclude voxels containing substantial amounts of cerebral spinal fluid (CSF). All of the ROIs included voxels from 26 slices, for each subject, that covered the majority of the cerebrum.

In order to obtain mean values for the model parameters, the voxels from the two subjects were pooled and voxelwise averages were computed. ROI 1 included a total of 1064 + 1412 = 2476 voxels from the two subjects, while ROI 2 had 13,156 + 12,178 = 25,334 voxels and ROI 3 had 14,176 + 13,307 = 27,483 voxels. For ROI 1, the kurtosis dODFs detected three or more fiber directions in 2.0% of the voxels, while for ROI 2, 3.4% of the voxels had three or more directions. Thus, most of the voxels considered were consistent with the assumptions of Example 2. The standard deviations for the full set of voxels corresponding to a given ROI were used to indicate the uncertainties in the mean values.

Numerical simulations

When the assumptions of a KANDO model differ from the true tissue properties, errors in the KANDO estimates for the model parameters can be expected. One such potential source of error is CSF contamination. To illustrate the potential effects of this, numerical simulations were performed for test models wherein CSF partial water fractions, f_{CSF}, were added with values ranging from 0 to 0.3. The diffusion for the CSF component was assumed to be isotropic with a diffusivity of 3.0 μm^2/ms. Three test models were constructed to be consistent with the assumptions of Examples 1, 2, and 3, except for the added CSF, and the model parameters were

then estimated using the KANDO method. In this way, the errors in the KANDO parameters caused by the CSF were determined.

For all three test models, D^* was set to 1.0 μm^2/ms. For the Example 1 test model, the three eigenvalues for $\mathbf{D}^{(0)}$ were chosen to be 2.0 μm^2/ms, 0.8 μm^2/ms, and 0.8 μm^2/ms, while the water fraction for the slack compartment was set to 0.5 (when $f_{CSF} = 0$). These values are similar to the results obtained by Fieremans and coworkers (Fieremans et al., 2011). For the Example 2 test model, the eigenvalues for $\mathbf{D}^{(0)}$ were chosen to be 1.4 μm^2/ms, 1.4 μm^2/ms, and 0.8 μm^2/ms, and the water fraction for the slack compartment was again set to 0.5. Two cases for Example 2 were considered, one in which $\mathbf{v}^{(1)}$ and $\mathbf{v}^{(2)}$ had a relative angle of 90° (Case A) and one in which $\mathbf{v}^{(1)}$ and $\mathbf{v}^{(2)}$ had a relative angle of 75° (Case B). In applying KANDO, these vectors were estimated from the kurtosis dODF, which can potentially yield directions that differ somewhat from those specified (Jensen et al., 2014a). For Example 3, all three test model eigenvalues for $\mathbf{D}^{(0)}$ were set to 1.2 μm^2/ms, so that the slack compartment was isotropic. Two cases were analyzed for Example 3, one with the true slack compartment water fraction set to 0.5 (Case A) and one with the slack compartment water fraction set to 2/3 (Case B).

For Example 3, as second set of simulations were performed in order to investigate the effect of a difference between the true and assumed values for intrinsic intra-neurite diffusivity D^*. For the test model, we set $D^* = D^*_{test}$ and considered values for D^*_{test} ranging from 0 to 2 μm^2/ms. In applying KANDO, the assumed value for D^* was 1 μm^2/ms, so that errors in the KANDO parameter estimates could be expected whenever $D^*_{test} \neq 1$. As for the first set of simulations, the test model eigenvalues for $\mathbf{D}^{(0)}$ were assumed to be 1.2 μm^2/ms. Both Case A, with the slack compartment water fraction set to 0.5, and Case B, with the slack compartment

water fraction set to 2/3, were analyzed. No CSF contamination was included for this second set of simulations.

A final set of simulations were performed for Example 3 in order to illustrate the difference between parameter estimates obtained with KANDO and those derived from a direct fit to the dMRI signal. The same two cases were examined, as for the simulation described above with a range of D^*_{test} values. The exact signal $S(b)$, for b-values of 0, 1000, and 2000 s/mm^2, was calculated from

$$S(b) = S(0)\left[f_0 \exp\left(-b\overline{D}_e\right) + (1- f_0)\sqrt{\frac{\pi}{4bD^*_{test}}}\,\mathrm{erf}\left(\sqrt{D^*_{test}b}\right)\right], \tag{38}$$

where $\overline{D}_e$ is the mean extra-neurite diffusivity (set, as above, to 1.2 μm^2/ms) and the term with the error function gives the signal for the neurite compartment in the thin cylinder limit (Yablonskiy and Sukstankii, 2010). Note that this signal is isotropic so that just a single diffusion direction need be considered. The DKI estimates for the total diffusivity and kurtosis are given by

$$D_{DKI} = \frac{b_2}{(b_2 - b_1)b_1}\ln\left[\frac{S(0)}{S(b_1)}\right] - \frac{b_1}{(b_2 - b_1)b_2}\ln\left[\frac{S(0)}{S(b_2)}\right], \tag{39}$$

and

$$K_{DKI} = \frac{6}{(b_2 - b_1)D^2_{DKI}}\left\{\frac{1}{b_1}\ln\left[\frac{S(0)}{S(b_1)}\right] - \frac{1}{b_2}\ln\left[\frac{S(0)}{S(b_2)}\right]\right\}, \tag{40}$$

where $b_1 = 1000$ s/mm^2 and $b_2 = 2000$ s/mm^2 (Jensen and Helpern, 2010). These estimates based on Eqs. (39) and (40) were used in order to simulate a real experimental procedure. Since they only approximate the true total diffusivity and kurtosis, some inaccuracy in the model

parameter estimates may be attributable to errors in D_{DKI} and K_{DKI}. However, this error could, in principle, be made arbitrarily small by adjusting the choice of b-values (Jensen and Helpern, 2010). The KANDO analysis for Cases A and B was performed exactly as for the simulations described in the previous paragraph, with $D^* = 1$ μm^2/ms, except that the prior calculations used exact rather than approximate values for the total diffusivity and kurtosis. The parameters estimates for a direct fit to the signal were obtained by minimizing

$$C_{signal} \equiv \left[S_{\mathrm{mod}}(b_1) - S(b_1)\right]^2 + \left[S_{\mathrm{mod}}(b_2) - S(b_2)\right]^2, \tag{41}$$

where

$$S_{\mathrm{mod}}(b) = S(0)\left[f_0 \exp\left(-b\overline{D}_e\right) + (1 - f_0)\sqrt{\frac{\pi}{4bD^*}}\,\mathrm{erf}\left(\sqrt{D^* b}\right)\right]. \tag{42}$$

The model signal $S_{\mathrm{mod}}(b)$ differs from the exact signal of Eq. (38) in that the intrinsic intra-neurite diffusivity has an assumed value of $D^* = 1$ μm^2/ms, while for the exact signal, the intra-neurite diffusivity ranges from $D^*_{test} = 0$ to 2 μm^2/ms. The minimization of C_{signal} has two free parameters, f_0 and $\overline{D}_e$, and was performed by an exhaustive search of parameter space. The number of free parameters is greater for the direct signal model fit than for the KANDO analysis because of the introduction of the slack compartment for KANDO.

Results

Human data

Table 1 shows the mean values, with standard deviations, over the three ROIs of selected model parameters computed for Examples 1, 2, and 3 based on the human DKI data. In Example 1, results for both the $K_{\max}$ and $K_{\perp,\max}$ options for calculating f_1 are given (see Eq. (11)). Also shown are results for ROI 1 obtained with the Fieremans model (Fieremans et al., 2011).

For all the models, the neurite water fraction is given by $1-f_0$. For Examples 1 and 2, as well as for the Fieremans model, the neurite water fraction is the same as the axonal water fraction, as there are no dendrites in white matter. For Example 1 and the Fieremans model, we also have $f_1 = 1-f_0$. The axonal water fraction for Example 1 with the $K_{\max}$ option is identical to the axonal water fraction for the Fieremans model. The extra-neurite mean diffusivities are calculated from $\overline{D}_e = Tr(\mathbf{D}^{(0)})/3$. For ROI 1, the extra-neurite axial diffusivity, $D_{e,\parallel}$, is equal to the largest eigenvalue of $\mathbf{D}^{(0)}$, while the extra-neurite radial diffusivity, $D_{e,\perp}$, is the average of the two smaller eigenvalues of $\mathbf{D}^{(0)}$. For ROI 2, $D_{e,\perp}$ corresponds to the smallest eigenvalue of $\mathbf{D}^{(0)}$, so that it indicates the diffusivity in a direction that is approximately perpendicular to any fiber crossings. Representative parametric maps for a single axial slice are displayed in Fig. 2.

The voxelwise average over ROI 1 of the ratio for f_1 as obtained with Eq. (11) using $K_{\max}$ to f_1 as obtained with Eq. (11) using $K_{\perp,\max}$ is 1.007 ± 0.011, indicating that there is little difference for these two approaches in voxels with unidirectional axonal bundles. The corresponding voxelwise averages for D^*, $\overline{D}_e$, $D_{e,\parallel}$, and $D_{e,\perp}$, as obtained using the Example 1 model, are 1.007 ± 0.013, 1.004 ± 0.008, 1.002 ± 0.004, and 1.007 ± 0.015 respectively. This close agreement suggests that the condition of Eq. (A21) is indeed satisfied for most voxels within ROI 1.

Although the f_1 value obtained using $K_{\max}$ in Eq. (11) is identical to the f_1 value for the Fieremans model, the D^*, $\overline{D}_e$, $D_{e,\parallel}$, and $D_{e,\perp}$ values for Example 1, using the $K_{\max}$ option, do differ somewhat from the predictions of the Fieremans model. The voxelwise averages over ROI 1 of the D^*, $\overline{D}_e$, $D_{e,\parallel}$, and $D_{e,\perp}$ ratios for these two models are 0.864 ± 0.115, 1.040 ± 0.037,

0.993 ± 0.054, and 1.113 ± 0.066. Thus the Fieremans model predicts higher D^* and $D_{e,\parallel}$ values and lower $\overline{D}_e$ and $D_{e,\perp}$ values, as is also shown by Table 1.

Numerical simulations

The effects of CSF contamination on the estimated neurite water fraction ($1-f_0$), the intrinsic intra-neurite diffusivity (D^*), and the mean extra-neurite diffusivity ($\overline{D}_e$=MDe) are shown in Fig. 3. All of these parameters are altered by the presence of CSF, with the exception of D^* for Example 3 which is constant by fiat. For the data plotted, the maximum absolute error for $1-f_0$ is 0.136 while the maximum relative error is 39%, the maximum absolute error for D^* is 0.221 μm^2/ms while the maximum relative error is 22%, and the maximum absolute error for $\overline{D}_e$ is 1.388 μm^2/ms while the maximum relative error is 116%. Thus of these parameters, the mean extra-neurite diffusivity is the most sensitive to CSF partial volume effects.

In Fig. 4, $1-f_0$, D^*, and $\overline{D}_e$ are plotted as functions of D^*_{test} for Example 3. For $D^* = D^*_{test}$ = 1.0 μm^2/ms, the KANDO estimates equal the true values. For the range 0.5 μm^2/ms ≤ D^*_{test} ≤ 1.5 μm^2/ms, the maximum absolute error for $1-f_0$ is 0.143 while the maximum relative error is 29%, the maximum absolute error for D^* is 0.5 μm^2/ms while the maximum relative error is 50%, and the maximum absolute error for $\overline{D}_e$ is 0.215 μm^2/ms while the maximum relative error is 18%. Not surprisingly, of the three estimated parameters, D^* has the largest relative error.

A comparison of $1-f_0$ and $\overline{D}_e$ estimates for Example 3 as obtained with KANDO and with a direct fit to the signal model of Eq. (42) are shown in Fig. 5. The signal model estimates agree with the true values when $D^*_{test} = D^*$, but the KANDO estimates have small errors due to

the use of the approximations of Eqs. (38) and (39) for the total diffusivity and kurtosis. When $D^*_{test} \neq D^*$, the estimates from both methods typically depart from the ideal values. The dependence of these errors on D^*_{test} is qualitatively similar for KANDO and the signal model fits, but is not identical due to the distinct mathematical formulations of the two approaches.

Discussion

The biophysical interpretation of dMRI data from brain is a challenging inverse problem that has been the subject of numerous studies and has employed a variety of tissue models (Novikov and Kiselev, 2010; Panagiotaki et al., 2012; Yablonskiiy and Sukstanskii, 2010). In this work, the special case of interpreting the information provided by just the kurtosis and diffusion tensors has been considered, which is specifically relevant for DKI. In order to further this goal, we have proposed the KANDO method. KANDO is a general computational framework that can accommodate non-exchanging, multiple Gaussian compartment models, as long as the number of model parameters does not exceed the number of independent parameters for the kurtosis tensor (which is 15 unless reduced by symmetry). KANDO is similar to conventional approaches that utilize tissue models in order to derive microstructural information directly from the dMRI signal (Assaf et al., 2004; Ferizi et al., 2013; Jespersen et al., 2007; Panagiotaki et al., 2009; Panagiotaki et al., 2012; Wang et al., 2011; White et al., 2013; Zhang et al., 2012). However, by applying modeling to the kurtosis tensor, rather than to the signal, KANDO facilitates the biophysical interpretation of this quantity, which may help to better understand the changes in kurtosis metrics that have been associated with neuropathology (Hori et al., 2012; Steven et al., 2014).

KANDO is an example of a modular approach to the modeling of dMRI data in that the acquisition of the signal and the tissue modeling are decoupled. The signal is used just to

estimate the kurtosis and diffusion tensors, which are well-defined physical quantities with no explicit connection to tissue microstructure. KANDO modeling then only uses these two tensors and does not directly involve imaging parameters, such as the diffusion gradient directions and b-values. Therefore results obtained with KANDO may depend less on the details of the imaging protocol and are potentially more reproducible between studies. Since the accuracy of the tensor measurements can be influenced by the choice of imaging parameters (Jensen and Helpern, 2010), there is still an indirect effect of the details of the imaging protocol on KANDO parameter estimates, but this can, in principle, be made arbitrarily small. This modular approach also supports the independent optimization of data acquisition and tissue modeling. Such a modular approach to the modeling is commonly employed for white matter fiber tractography, where the diffusion tensor or the dODF is the physical quantity directly estimated from the dMRI signal (Lazar, 2010). However, modular approaches have been less frequently applied in the context of multiple Gaussian compartment modeling of the microscopic diffusion organization in neural tissue. Note that KANDO's modular structure means that the components of measured diffusion and kurtosis tensors are distinguished from the model parameters and regarded as inputs for KANDO rather than adjustable parameters. By design, the number of model parameters for KANDO equals the number of adjustable parameters determined by minimizing the cost function of Eq. (9).

By only utilizing the kurtosis and diffusion tensors some of the information contained in the dMRI signal is in effect discarded from the analysis. However, the kurtosis and diffusion tensors contain the majority of the information obtainable with small diffusion weightings (Jensen and Helpern, 2010), and so this loss is likely to be minor when low b-value dMRI methods, such as DKI, are employed. In addition, by basing the modeling solely on these two

tensors, KANDO can benefit from the advanced post-processing methods already available for DKI (André et al., 2014; Ghosh et al., 2014; Glenn et al., 2014; Kuder et al., 2012; Tabesh et al., 2011; Masutani and Aoki, 2014; Poot et al., 2010; Tax et al., 2014; Veraart et al., 2013; Veraart et al., 2011).

KANDO is closely related to the previously proposed method of Fieremans and coworkers (Fieremans et al., 2011) that utilizes DKI to model microstructure in white matter with unidirectional axons. Indeed, the results obtained with Example 1 are quite similar to those for the Fieremans method (see Table 1). Operationally, the Fieremans approach differs from KANDO in that it avoids nonlinear optimization by instead solving a set of algebraic equations, which leads to a simple and efficient numerical method. However, this algebraic technique is not readily generalizable to more complex cytoarchitectures, as found in white matter with fiber crossings and in gray matter, which is a primary motivation for developing KANDO. It should also be mentioned that in applying the Fieremans method, one typically obtains two formal mathematical solutions (one with $D^* < \lambda_1$ and one with $D^* > \lambda_1$), with an independent argument being invoked to select one as the most likely to be physically relevant. With KANDO, such ancillary considerations are entirely avoided. The correctness of the chosen solution for Fieremans approach is supported by the close agreement between the Fieremans and KANDO results of Example 1.

In order to illustrate KANDO, we have given results for three simple models. Example 1 is essentially a reformulation of the Fieremans white matter model in terms of KANDO and is only suitable for white matter regions, such as the corpus callosum, for which the axons are largely unidirectional. Example 2 is a more general model that allows for fiber crossings and is potentially applicable throughout much of the white matter. Example 3 assumes the intra-neurite

space is isotropic, as appropriate for many gray matter regions. The nonlinear optimization calculations for Examples 1 and 3 involve only a single free parameter, while the optimization for Example 2 involves two free parameters. Because of this small number of variables, the numerical minimization of the cost function can be easily accomplished with an exhaustive search of parameter space that mitigates potential issues with local minima. However, an exhaustive search might not be feasible for more complex models that require additional free parameters. In such cases, alternative optimization procedures may be needed.

For the white matter models of Examples 1 and 2, the small number of free parameters is partly due to the application of Eqs. (11) and (19) that give the axonal water fraction in terms of the kurtosis. As discussed in the Appendix, these formulae are a consequence of the thin cylinder approximation for axons, so that intra-voxel diffusivity perpendicular to the cylinder axis is taken to be zero. For voxels regarded as having a single fiber direction, there is a question as to whether it is best to use the maximum of the kurtosis over all directions or over just directions perpendicular to the cylinder axis, as discussed in the Appendix. For the algebraic approach of Fieremans, one may show that choosing the global maximum option is logically consistent with the aforementioned selection of one of two formal mathematical solutions. The same reasoning does not necessarily apply to the KANDO examples considered here, as the ancillary assumptions included with the Fieremans approach are absent from KANDO. For this reason, we have also considered the use of the kurtosis optimized over perpendicular directions. As demonstrated in the Appendix, the conditions for the validity of this alternative are less demanding than for the global option. One may hence suppose the perpendicular option to be the more robust choice for the KANDO white matter models of Examples 1 and 2. Nonetheless, our

Example 1 results for human brain show that there is little actual difference in the estimated axonal water fractions (see Table 1 and Fig. 2).

For the gray matter model of Example 3, it is not possible to predict the neurite water fraction directly from the kurtosis, as there is no direction that is orthogonal to all the neurites. Therefore, the neurite water fraction is treated as a free parameter that is determined from minimization of the cost function C. This is the only free parameter for Example 3, and in contrast to Examples 1 and 2, the intrinsic intra-neurite diffusivity D^* is regarded as a given input. Fixing the intrinsic intra-neurite diffusivity is necessary, because for isotropic geometries the information content of the kurtosis tensor drops from 15 independent parameters to just a single parameter (as the kurtosis is the same in all directions). For the results presented in this work, we set $D^* = 1.0$ μm^2/ms. However, future work may suggest alternative values. For example, one might set the gray matter D^* equal to the value found with KANDO modeling in adjacent white matter regions, for which D^* need not be set a priori. Ex vivo experiments suggest that D^* may be similar for white and gray matter (Jespersen et al., 2007). However, for brain with focal gray matter pathology, the need specify a value for D^* may preclude the use of models such as that of Example 3.

For Examples 1 and 2, it is probably well justified to regard water within myelinated axons to be part of the water pool captured by the parameter $1-f_0$, as water exchange times for myelinated axons are likely to be long in comparison with typical dMRI diffusion times (Nilsson et al., 2013). However, some white matter axons are not myelinated, and it is less clear to what degree their water will contribute to $1-f_0$. For gray matter, the situation is even more nebulous as little is known about water exchange times for dendrites and gray matter axons, which are mostly unmyelinated. Thus the neurite water fraction calculated with KANDO should be

interpreted as an effective water fraction representing water that remains inside the neurites during the diffusion time interval of the dMRI experiment. Indeed, our measured values for $1-f_0$ are significantly smaller than neurite volume fractions for gray matter determined from histology (Chklovskii et al., 2002). This could be due to a discrepancy between our choice for D^* and the true intra-neurite diffusivity, to water exchange between the intra- and extra-neurite spaces, or to a combination of these two possibilities. This illustrates the caution needed when interpreting parameter estimates obtained with KANDO, as with most other dMRI modeling methods.

Particular care should also be exercised when interpreting estimates of D^* for Examples 1 and 2, as these may be affected by differences between the assumed and true axonal geometries. For instance, applying the model of Example 1 to a fiber bundle with significant curvature may yield systematically low values for D^*, as axonal curvature can restrict the intra-neurite diffusion in the direction of the principal diffusion tensor eigenvector.

Another assumption of the examples considered here is that the extra-neurite space can be treated as a single Gaussian compartment. This presupposes that the diffusion restrictions due to glial cell membranes are not sufficient to generate a substantial intrinsic kurtosis. Again there is limited hard evidence to support this, although astrocytes are known to express aquaporin 4, which may significantly increase their plasma membrane permeability (Badaut et al., 2011; Solenov et al., 2004).

The three specific models discussed in this paper were chosen primarily as simple illustrations of KANDO. The KANDO framework can also be applied to many other similar models, including a large fraction of those considered in prior studies. The main difference is that, with KANDO, the only experimental inputs are the kurtosis and diffusion tensors, while

most prior applications of multiple Gaussian compartment models have used fits to the full dMRI signal to determine the free parameters, as illustrated by the results of Fig. 5. Further comparisons of KANDO with conventional approaches based on the dMRI signal, for equivalent tissue models, would be an interesting topic of investigation.

A crucial issue for KANDO, as well as other dMRI modeling approaches, is independent validation of the model predictions. One method is to compare estimated compartmental water fractions with histologically determined volume fractions. For instance, the axonal water fractions obtained with Examples 1 and 2 should be approximately related to the axonal volume fraction by

$$f_{axon} = \frac{V_{axon}}{1 - V_{myelin}} \ , \tag{43}$$

where V_{axon} is the axonal volume fraction and V_{myelin} is the myelin volume fraction. The denominator in Eq. (43) is needed to take into account the fact that myelin water usually contributes little to the dMRI signal due to the short T2 of myelin (Stanisz et al, 1999). Stereological studies have estimated the myelinated axonal volume fraction in (human) white matter to be 0.33 ± 0.02 (Tang et al., 1997) and the myelin volume fraction in (rat) white matter to be 0.22 ± 0.02 (Yang et al., 2008). Applying these numbers to Eq. (43) yields $f_{axon} = 0.42 \pm 0.03$, which is indeed similar to the result of $f_{axon} = 1 - f_0 = 0.405 \pm 0.066$ obtained here with KANDO for Example 2 and RO1 2 (see Table 1). Nevertheless, a direct comparison of KANDO estimates to histological results for the same brain tissue would be more compelling.

Aside from the compartment water fractions, the parameters estimated with KANDO all pertain to the microscopic organization of the diffusion environment, as encompassed by the compartmental diffusion tensors and associated quantities. Since these cannot be validated

directly with histology, alternative techniques are required. One method is to utilize numerical simulations to test the accuracy KANDO models, as illustrated by the results of Figs. 3 and 4. These calculations suggest, for example, that the effects of CSF partial voluming on KANDO parameter estimates are most pronounced for the extra-neurite diffusivity. Similar numerical methods have frequently been applied to the study of other dMRI tissue models (Fieremans et al., 2010; Jespersen et al., 2007; Novikov and Kiselev, 2010; Yablonskiy and Sukstanskii, 2010).

Another approach is to experimentally test the model predictions for the dMRI signal behavior at higher b-values (typically $b \geq 3000$ s/mm^2) than those used for obtaining the kurtosis and diffusion tensors (Fieremans et al., 2011). However, if standard single pulsed dMRI is employed, disparate tissue models can yield similar or, in principle, even identical dMRI signals for the full range of b-values. As a consequence, consistency between a model's predictions and high b-value data alone may not always provide a satisfactory level of verification. For additional validation of KANDO, double pulsed dMRI could be employed (Jensen et al., 2014b; Lawrenz and Finsterbusch, 2013; Shemesh et al., 2010). Double pulsed dMRI yields independent diffusion information not obtainable with single pulsed dMRI and is particularly sensitive to microscopic anisotropy, as can result from fiber crossings.

Conclusion

KANDO is a computational framework for tissue modeling that uses the kurtosis and diffusion tensors as inputs. It accommodates non-exchanging, multiple Gaussian compartment models and may help to delineate the microscopic diffusion organization of neural tissue. KANDO is particularly suitable as an adjunct to DKI and can be applied to improve the biophysical interpretability of DKI-derived diffusion metrics. In addition, parameters estimated

with KANDO may serve as candidate biomarkers for neurological disorders in which neural microstructure is altered.

Acknowledgments

We are grateful to Ali Tabesh for helpful discussions. This work was supported by National Institutes of Health research grant 1R21NS085475 (to J.H.J.) and the Litwin Foundation (to J.A.H.).

Appendix

Here we derive general results for the water fraction of a diffusion compartment with a vanishing diffusivity for at least one direction. These are applicable to white matter models for which the axons idealized as thin cylinders and are assumed to have coplanar orientations within each voxel.

Consider a system consisting of two non-exchanging, but not necessarily Gaussian, compartments *A* and *B*, with diffusivities $D_A(\mathbf{n})$ and $D_B(\mathbf{n})$ and kurtoses $K_A(\mathbf{n})$ and $K_B(\mathbf{n})$ for the diffusion direction $\mathbf{n}$. Let us also define moments for compartments *A* and *B* as

$$M_{\alpha,A}(\mathbf{n}) = \left\langle (\mathbf{r}\cdot\mathbf{n})^{\alpha} \right\rangle_A \tag{A.1}$$

and

$$M_{\alpha,B}(\mathbf{n}) = \left\langle (\mathbf{r}\cdot\mathbf{n})^{\alpha} \right\rangle_B , \tag{A.2}$$

where $\mathbf{r}$ is a diffusion displacement vector and the angle brackets $\langle \ldots \rangle_A$ and $\langle \ldots \rangle_B$ represent an averaging over the ensemble of water molecules in compartments *A* and *B*, respectively. The moments for the total system are related to the compartmental moments by

$$M_{\alpha}(\mathbf{n}) \equiv \left\langle (\mathbf{r}\cdot\mathbf{n})^{\alpha} \right\rangle = f_A M_{\alpha,A}(\mathbf{n}) + (1 - f_A) M_{\alpha,B}(\mathbf{n}), \tag{A.3}$$

with f_A being the water fraction for compartment *A* and with $\langle \ldots \rangle$ representing an averaging over the full ensemble of water molecules.

The compartmental diffusivities and kurtoses are defined by these moments according to

$$D_A(\mathbf{n}) = \frac{1}{2t} M_{2,A}(\mathbf{n}) \,, \tag{A.4}$$

$$D_B(\mathbf{n}) = \frac{1}{2t} M_{2,B}(\mathbf{n}) \,, \tag{A.5}$$

$$K_A(\mathbf{n}) = \frac{M_{4,A}(\mathbf{n})}{\left[M_{2,A}(\mathbf{n})\right]^2} - 3 \,, \tag{A.6}$$

and

$$K_B(\mathbf{n}) = \frac{M_{4,B}(\mathbf{n})}{\left[M_{2,B}(\mathbf{n})\right]^2} - 3 \,, \tag{A.7}$$

where t is the diffusion time (Jensen and Helpern, 2010). Similarly, the total diffusivity and kurtosis are defined by

$$D(\mathbf{n}) = \frac{1}{2t} M_2(\mathbf{n}) \tag{A.8}$$

and

$$K(\mathbf{n}) = \frac{M_4(\mathbf{n})}{\left[M_2(\mathbf{n})\right]^2} - 3. \tag{A.9}$$

As a consequence, one may easily verify that

$$D(\mathbf{n}) = f_A D_A(\mathbf{n}) + (1 - f_A) D_B(\mathbf{n}) \tag{A.10}$$

and that

$$\left[K(\mathbf{n}) + 3\right] \cdot \left[D(\mathbf{n})\right]^2 = f_A \left[K_A(\mathbf{n}) + 3\right] \cdot \left[D_A(\mathbf{n})\right]^2 + (1 - f_A) \left[K_B(\mathbf{n}) + 3\right] \cdot \left[D_B(\mathbf{n})\right]^2 . \tag{A.11}$$

If we assume that $D_A(\mathbf{n})$ vanishes for a particular diffusion direction $\mathbf{n}=\mathbf{n}'$, then Eqs. (A.10) and (A.11) in this direction reduce to

$$D(\mathbf{n}')=(1-f_A)D_B(\mathbf{n}') \tag{A.12}$$

and

$$[K(\mathbf{n}')+3]\cdot[D(\mathbf{n}')]^2=(1-f_A)[K_B(\mathbf{n}')+3]\cdot[D_B(\mathbf{n}')]^2. \tag{A.13}$$

This in turn implies

$$f_A=\frac{K(\mathbf{n}')-K_B(\mathbf{n}')}{K(\mathbf{n}')+3}. \tag{A.14}$$

For the special case that compartment *B* is Gaussian, we then have $K_B(\mathbf{n})=0$ and

$$f_A=\frac{K(\mathbf{n}')}{K(\mathbf{n}')+3}. \tag{A.15}$$

By regarding compartment *B* as the slack compartment for KANDO, Eq. (A.15) forms the basis of Eqs. (11) and (19). Note that compartment A is here taken to represent the ensemble of all the KANDO compartments with $n\geq 1$.

For white matter models that idealize axons as thin cylinders, the $\mathbf{n}'$ direction should be chosen so as to be perpendicular to all the axons, as the diffusivity is formally zero in this direction due to the thin cylinder approximation. If there are two crossing fiber directions, then $\mathbf{n}'$ is the unique direction orthogonal to both of these directions.

When only a single fiber direction is detected, the best choice of $\mathbf{n}'$ is not completely clear-cut, since there are infinitely many directions orthogonal to the fiber bundle for which Eq. (A.15) could, in principle, be applied. To motivate a specific $\mathbf{n}'$ for practical calculations,

we set $K_B(\mathbf{n})=0$, as is appropriate for the slack compartment, in which case Eq. (A.11) reduces to

$$[K(\mathbf{n})+3]\cdot[D(\mathbf{n})]^2 = f_A[K_A(\mathbf{n})+3]\cdot[D_A(\mathbf{n})]^2 + 3(1-f_A)[D_B(\mathbf{n})]^2 . \quad \text{(A.16)}$$

By using Eq. (A.10) to eliminate $D_B(\mathbf{n})$, one finds

$$[K(\mathbf{n})+3]\cdot[D(\mathbf{n})]^2 = f_A[K_A(\mathbf{n})+3]\cdot[D_A(\mathbf{n})]^2 + \frac{3}{(1-f_A)}[D(\mathbf{n})-f_A D_A(\mathbf{n})]^2 . \quad \text{(A.17)}$$

This is easily rearranged to give

$$K(\mathbf{n}) = \frac{3f_A[D(\mathbf{n})-D_A(\mathbf{n})]^2}{(1-f_A)[D(\mathbf{n})]^2} + f_A K_A(\mathbf{n})\left[\frac{D_A(\mathbf{n})}{D(\mathbf{n})}\right]^2 . \quad \text{(A.18)}$$

If $D_A(\mathbf{n})$ is near zero, then Eq. (A.18) has the linear approximation

$$K(\mathbf{n}) \approx \frac{3f_A}{(1-f_A)} - \frac{6f_A}{(1-f_A)}\frac{D_A(\mathbf{n})}{D(\mathbf{n})} + O\{[D_A(\mathbf{n})]^2\}. \quad \text{(A.19)}$$

Thus in the neighborhood of $\mathbf{n}=\mathbf{n}'$, there is a local maximum in the total kurtosis given by

$$K_{\max} = \frac{3f_A}{(1-f_A)} . \quad \text{(A.20)}$$

Moreover, this will also be a global maximum provided

$$D_A(\mathbf{n}) \le \frac{6D(\mathbf{n})}{3+(1-f_A)K_A(\mathbf{n})} \quad \text{(A.21)}$$

for all directions $\mathbf{n}$. If the kurtosis for compartment *A* is small in comparison to one, as would be the case if *A* consists thin cylinders that are all nearly aligned with each other, then the condition of Eq. (A.21) is essentially $D_A(\mathbf{n}) \le 2D(\mathbf{n})$, which may be normally expected to hold in white matter, as the intra-axonal diffusivity has usually been estimated as small or comparable to the total diffusivity. By inverting Eq. (A.20), one finds

$$f_A = \frac{K_{\max}}{K_{\max} + 3}, \tag{A.22}$$

which matches the result of Eq. (1) and has been previously applied by Fieremans and coworkers (Fieremans et al., 2011). More conservatively, one could use the maximum perpendicular kurtosis, $K_{\perp,\max}$, obtained by only considering directions orthogonal to the estimated fiber direction, which leads to the estimate

$$f_A = \frac{K_{\perp,\max}}{K_{\perp,\max} + 3}. \tag{A.23}$$

Applied to KANDO modeling of white matter, Eqs. (A.22) and (A.23) should, in most cases, give comparable results. However, Eq. (A.23) may be more foolproof, since the condition of Eq. (A.21) is less likely to be violated due to $D_A(\mathbf{n})$ generally being small for all orthogonal directions.

References

Adisetiyo V, Tabesh A, Di Martino A, Falangola MF, Castellanos FX, Jensen JH, Helpern JA. Attention-deficit/hyperactivity disorder without comorbidity is associated with distinct atypical patterns of cerebral microstructural development. Hum Brain Mapp. 2014 May;35(5):2148-62.

Alexander DC, Barker GJ, Arridge SR. Detection and modeling of non-Gaussian apparent diffusion coefficient profiles in human brain data. Magn Reson Med. 2002 Aug;48(2):331-40.

André ED, Grinberg F, Farrher E, Maximov II, Shah NJ, Meyer C, Jaspar M, Muto V, Phillips C, Balteau E. Influence of noise correction on intra- and inter-subject variability of quantitative metrics in diffusion kurtosis imaging. PLoS One. 2014 Apr 10;9(4):e94531.

Assaf Y, Freidlin RZ, Rohde GK, Basser PJ. New modeling and experimental framework to characterize hindered and restricted water diffusion in brain white matter. Magn Reson Med. 2004 Nov;52(5):965-78.

Badaut J, Ashwal S, Adami A, Tone B, Recker R, Spagnoli D, Ternon B, Obenaus A. Brain water mobility decreases after astrocytic aquaporin-4 inhibition using RNA interference. J Cereb Blood Flow Metab. 2011 Mar;31(3):819-31.

Benitez A, Fieremans E, Jensen JH, Falangola MF, Tabesh A, Ferris SH, Helpern JA. White matter tract integrity metrics reflect the vulnerability of late-myelinating tracts in Alzheimer's disease. Neuroimage Clin. 2014 Jan;4:64-71.

Cheung JS, Wang E, Lo EH, Sun PZ. Stratification of heterogeneous diffusion MRI ischemic lesion with kurtosis imaging: evaluation of mean diffusion and kurtosis MRI mismatch in an animal model of transient focal ischemia. Stroke. 2012 Aug;43(8):2252-4.

Chklovskii DB, Schikorski T, Stevens CF. Wiring optimization in cortical circuits. Neuron. 2002 Apr 25;34(3):341-7.

Falangola MF, Jensen JH, Tabesh A, Hu C, Deardorff RL, Babb JS, Ferris S, Helpern JA. Non-Gaussian diffusion MRI assessment of brain microstructure in mild cognitive impairment and Alzheimer's disease. Magn Reson Imaging. 2013 Jul;31(6):840-6.

Ferizi U, Schneider T, Panagiotaki E, Nedjati-Gilani G, Zhang H, Wheeler-Kingshott CA, Alexander DC. A ranking of diffusion MRI compartment models with in vivo human brain data. Magn Reson Med. 2013 Dec 17. doi: 10.1002/mrm.25080.

Fieremans E, Benitez A, Jensen JH, Falangola MF, Tabesh A, Deardorff RL, Spampinato MV, Babb JS, Novikov DS, Ferris SH, Helpern JA. Novel white matter tract integrity metrics sensitive to Alzheimer disease progression. AJNR Am J Neuroradiol. 2013 Nov-Dec;34(11):2105-12.

Fieremans E, Jensen JH, Helpern JA. White matter characterization with diffusional kurtosis imaging. Neuroimage. 2011 Sep 1;58(1):177-88.

Fieremans E, Novikov DS, Jensen JH, Helpern JA. Monte Carlo study of a two-compartment exchange model of diffusion. NMR Biomed. 2010 Aug;23(7):711-24.

Gao Y, Zhang Y, Wong CS, Wu PM, Zhang Z, Gao J, Qiu D, Huang B. Diffusion abnormalities in temporal lobes of children with temporal lobe epilepsy: a preliminary diffusional kurtosis imaging study and comparison with diffusion tensor imaging. NMR Biomed. 2012 Dec;25(12):1369-77.

Ghosh A, Milne T, Deriche R. Constrained diffusion kurtosis imaging using ternary quartics & MLE. Magn Reson Med. 2014 Apr;71(4):1581-91.

Glenn GR, Tabesh A, Jensen JH. A simple noise correction scheme for diffusional kurtosis imaging. Magn Reson Imaging. 2014 Aug 27. doi: 10.1016/j.mri.2014.08.028.

Gong NJ, Wong CS, Chan CC, Leung LM, Chu YC. Correlations between microstructural alterations and severity of cognitive deficiency in Alzheimer's disease and mild cognitive impairment: a diffusional kurtosis imaging study. Magn Reson Imaging. 2013 Jun;31(5):688-94.

Gong NJ, Wong CS, Chan CC, Leung LM, Chu YC. Aging in deep gray matter and white matter revealed by diffusional kurtosis imaging. Neurobiol Aging. 2014 Oct;35(10):2203-16.

Grossman EJ, Ge Y, Jensen JH, Babb JS, Miles L, Reaume J, Silver JM, Grossman RI, Inglese M. Thalamus and cognitive impairment in mild traumatic brain injury: a diffusional kurtosis imaging study. J Neurotrauma. 2012 Sep;29(13):2318-27.

Grossman EJ, Jensen JH, Babb JS, Chen Q, Tabesh A, Fieremans E, Xia D, Inglese M, Grossman RI. Cognitive impairment in mild traumatic brain injury: a longitudinal diffusional kurtosis and perfusion imaging study. AJNR Am J Neuroradiol. 2013 May;34(5):951-7, S1-3.

Helpern JA, Adisetiyo V, Falangola MF, Hu C, Di Martino A, Williams K, Castellanos FX, Jensen JH. Preliminary evidence of altered gray and white matter microstructural development in the frontal lobe of adolescents with attention-deficit hyperactivity disorder: a diffusional kurtosis imaging study. J Magn Reson Imaging. 2011 Jan;33(1):17-23.

Holz M, Heil SR, Sacco A. Temperature-dependent self-diffusion coefficients of water and six selected molecular liquids for calibration in accurate 1H NMR PFG measurements. Phys Chem Chem Phys. 2000; 2(20): 4740-4742.

Hori M, Fukunaga I, Masutani Y, Taoka T, Kamagata K, Suzuki Y, Aoki S. Visualizing non-Gaussian diffusion: clinical application of q-space imaging and diffusional kurtosis imaging of the brain and spine. Magn Reson Med Sci. 2012;11(4):221-33.

Hui ES, Fieremans E, Jensen JH, Tabesh A, Feng W, Bonilha L, Spampinato MV, Adams R, Helpern JA. Stroke assessment with diffusional kurtosis imaging. Stroke. 2012 Nov;43(11):2968-73.

Jensen JH, Falangola MF, Hu C, Tabesh A, Rapalino O, Lo C, Helpern JA. Preliminary observations of increased diffusional kurtosis in human brain following recent cerebral infarction. NMR Biomed. 2011 Jun;24(5):452-7.

Jensen JH, Helpern JA. MRI quantification of non-Gaussian water diffusion by kurtosis analysis. NMR Biomed. 2010 Aug;23(7):698-710.

Jensen JH, Helpern JA, Ramani A, Lu H, Kaczynski K. Diffusional kurtosis imaging: the quantification of non-Gaussian water diffusion by means of magnetic resonance imaging. Magn Reson Med. 2005 Jun;53(6):1432-40.

Jensen JH, Helpern JA, Tabesh A. Leading non-Gaussian corrections for diffusion orientation distribution function. NMR Biomed. 2014a Feb;27(2):202-11.

Jensen JH, Hui ES, Helpern JA. Double-pulsed diffusional kurtosis imaging. NMR Biomed. 2014b Apr;27(4):363-70.

Jespersen SN, Kroenke CD, Østergaard L, Ackerman JJ, Yablonskiy DA. Modeling dendrite density from magnetic resonance diffusion measurements. Neuroimage. 2007 Feb 15;34(4):1473-86.

Kamagata K, Tomiyama H, Hatano T, Motoi Y, Abe O, Shimoji K, Kamiya K, Suzuki M, Hori M, Yoshida M, Hattori N, Aoki S. A preliminary diffusional kurtosis imaging study of

Parkinson disease: comparison with conventional diffusion tensor imaging. Neuroradiology. 2014 Mar;56(3):251-8.

Kamagata K, Tomiyama H, Motoi Y, Kano M, Abe O, Ito K, Shimoji K, Suzuki M, Hori M, Nakanishi A, Kuwatsuru R, Sasai K, Aoki S, Hattori N. Diffusional kurtosis imaging of cingulate fibers in Parkinson disease: comparison with conventional diffusion tensor imaging. Magn Reson Imaging. 2013 Nov;31(9):1501-6.

Kuder TA, Stieltjes B, Bachert P, Semmler W, Laun FB. Advanced fit of the diffusion kurtosis tensor by directional weighting and regularization. Magn Reson Med. 2012 May;67(5):1401-11.

Lawrenz M, Finsterbusch J. Double-wave-vector diffusion-weighted imaging reveals microscopic diffusion anisotropy in the living human brain. Magn Reson Med. 2013 Apr;69(4):1072-82.

Lazar M. Mapping brain anatomical connectivity using white matter tractography. NMR Biomed. 2010 Aug;23(7):821-35.

Lazar M, Jensen JH, Xuan L, Helpern JA. Estimation of the orientation distribution function from diffusional kurtosis imaging. Magn Reson Med. 2008 Oct;60(4):774-81.

Lazar M, Miles LM, Babb JS, Donaldson JB. Axonal deficits in young adults with High Functioning Autism and their impact on processing speed. Neuroimage Clin. 2014 Feb 7;4:417-25.

Lee CY, Tabesh A, Benitez A, Helpern JA, Jensen JH, Bonilha L. Microstructural integrity of early- versus late-myelinating white matter tracts in medial temporal lobe epilepsy. Epilepsia. 2013 Oct;54(10):1801-9.

Lee CY, Tabesh A, Spampinato MV, Helpern JA, Jensen JH, Bonilha L. Diffusional kurtosis imaging reveals a distinctive pattern of microstructural alternations in idiopathic generalized epilepsy. Acta Neurol Scand. 2014 Sep;130(3):148-55.

Masutani Y, Aoki S. Fast and Robust Estimation of Diffusional Kurtosis Imaging (DKI) Parameters by General Closed-form Expressions and their Extensions. Magn Reson Med Sci. 2014 Jun 23;13(2):97-115.

Nilsson M, Lätt J, van Westen D, Brockstedt S, Lasič S, Ståhlberg F, Topgaard D. Noninvasive mapping of water diffusional exchange in the human brain using filter-exchange imaging. Magn Reson Med. 2013 Jun;69(6):1573-81.

Novikov DS, Kiselev VG. Effective medium theory of a diffusion-weighted signal. NMR Biomed. 2010 Aug;23(7):682-97.

Panagiotaki E, Fonteijn H, Siow B, Hall MG, Price A, Lythgoe MF, Alexander DC. Two-compartment models of the diffusion MR signal in brain white matter. Med Image Comput Comput Assist Interv. 2009;12(Pt 1):329-36.

Panagiotaki E, Schneider T, Siow B, Hall MG, Lythgoe MF, Alexander DC. Compartment models of the diffusion MR signal in brain white matter: a taxonomy and comparison. Neuroimage. 2012 Feb 1;59(3):2241-54.

Poot DH, den Dekker AJ, Achten E, Verhoye M, Sijbers J. Optimal experimental design for diffusion kurtosis imaging. IEEE Trans Med Imaging. 2010 Mar;29(3):819-29.

Raab P, Hattingen E, Franz K, Zanella FE, Lanfermann H. Cerebral gliomas: diffusional kurtosis imaging analysis of microstructural differences. Radiology. 2010 Mar;254(3):876-81.

Rudrapatna SU, Wieloch T, Beirup K, Ruscher K, Mol W, Yanev P, Leemans A, van der Toorn A, Dijkhuizen RM. Can diffusion kurtosis imaging improve the sensitivity and specificity

of detecting microstructural alterations in brain tissue chronically after experimental stroke? Comparisons with diffusion tensor imaging and histology. Neuroimage. 2014 Aug 15;97:363-73.

Shemesh N, Ozarslan E, Komlosh ME, Basser PJ, Cohen Y. From single-pulsed field gradient to double-pulsed field gradient MR: gleaning new microstructural information and developing new forms of contrast in MRI. NMR Biomed. 2010 Aug;23(7):757-80.

Signoretto M, De Lathauwer L, Suykens JA. A kernel-based framework to tensorial data analysis. Neural Netw. 2011 Oct;24(8):861-74.

Solenov E, Watanabe H, Manley GT, Verkman AS. Sevenfold-reduced osmotic water permeability in primary astrocyte cultures from AQP-4-deficient mice, measured by a fluorescence quenching method. Am J Physiol Cell Physiol. 2004 Feb;286(2):C426-32.

Stanisz GJ, Kecojevic A, Bronskill MJ, Henkelman RM. Characterizing white matter with magnetization transfer and T(2). Magn Reson Med. 1999 Dec;42(6):1128-36.

Steven AJ, Zhuo J, Melhem ER. Diffusion kurtosis imaging: an emerging technique for evaluating the microstructural environment of the brain. AJR Am J Roentgenol. 2014 Jan;202(1):W26-33.

Tabesh A, 2012. Diffusional Kurtosis Estimator (nitrc.org/projects/dke).

Tabesh A, Jensen JH, Ardekani BA, Helpern JA. Estimation of tensors and tensor-derived measures in diffusional kurtosis imaging. Magn Reson Med. 2011 Mar;65(3):823-36.

Tang Y, Nyengaard JR, Pakkenberg B, Gundersen HJ. Age-induced white matter changes in the human brain: a stereological investigation. Neurobiol Aging. 1997 Nov-Dec;18(6):609-15.

Tax CM, Otte WM, Viergever MA, Dijkhuizen RM, Leemans A. REKINDLE: Robust extraction of kurtosis indices with linear estimation. Magn Reson Med. 2014 Mar 31. doi: 10.1002/mrm.25165.

Tuch DS. Q-ball imaging. Magn Reson Med. 2004 Dec;52(6):1358-72.

Van Cauter S, Veraart J, Sijbers J, Peeters RR, Himmelreich U, De Keyzer F, Van Gool SW, Van Calenbergh F, De Vleeschouwer S, Van Hecke W, Sunaert S. Gliomas: diffusion kurtosis MR imaging in grading. Radiology. 2012 May;263(2):492-501.

Veraart J, Rajan J, Peeters RR, Leemans A, Sunaert S, Sijbers J. Comprehensive framework for accurate diffusion MRI parameter estimation. Magn Reson Med. 2013 Oct;70(4):972-84.

Veraart J, Van Hecke W, Sijbers J. Constrained maximum likelihood estimation of the diffusion kurtosis tensor using a Rician noise model. Magn Reson Med. 2011 Sep;66(3):678-86.

Wang Y, Wang Q, Haldar JP, Yeh FC, Xie M, Sun P, Tu TW, Trinkaus K, Klein RS, Cross AH, Song SK. Quantification of increased cellularity during inflammatory demyelination. Brain. 2011 Dec;134(Pt 12):3590-601.

Wedeen VJ, Hagmann P, Tseng WY, Reese TG, Weisskoff RM. Mapping complex tissue architecture with diffusion spectrum magnetic resonance imaging. Magn Reson Med. 2005 Dec;54(6):1377-86.

White NS, Leergaard TB, D'Arceuil H, Bjaalie JG, Dale AM. Probing tissue microstructure with restriction spectrum imaging: Histological and theoretical validation. Hum Brain Mapp. 2013 Feb;34(2):327-46.

Wu EX, Cheung MM. MR diffusion kurtosis imaging for neural tissue characterization. NMR Biomed. 2010 Aug;23(7):836-48.

Yablonskiy DA, Sukstanskii AL. Theoretical models of the diffusion weighted MR signal. NMR Biomed. 2010 Aug;23(7):661-81.

Yang S, Li C, Zhang W, Wang WW, Nyengaard JR, Tang Y. Application of stereological method to study the white matter and myelinated fibers therein of rat brain. Image Anal Stereol. 2008; 27:125-132.

Zhang H, Schneider T, Wheeler-Kingshott CA, Alexander DC. NODDI: practical in vivo neurite orientation dispersion and density imaging of the human brain. Neuroimage. 2012 Jul 16;61(4):1000-16.

Zhang Y, Yan X, Gao Y, Xu D, Wu J, Li Y. A preliminary study of epilepsy in children using diffusional kurtosis imaging. Clin Neuroradiol. 2013 Dec;23(4):293-300.

Zhuo J, Xu S, Proctor JL, Mullins RJ, Simon JZ, Fiskum G, Gullapalli RP. Diffusion kurtosis as an in vivo imaging marker for reactive astrogliosis in traumatic brain injury. Neuroimage. 2012 Jan 2;59(1):467-77.

Figure captions

Figure 1: Schematic illustrating the fiber orientations utilized for Examples 1, 2 and 3. For Example 1, the axonal fibers within a given voxel are taken to be unidirectional. Intersecting fiber bundles are allowed in Example 2, with up to two distinct directions as determined from the kurtosis dODF. An isotropic distribution of axon and dendrite orientations is assumed for Example 3, so that all directions are equally probable.

Figure 2: Standard DKI images and KANDO maps for a single axial slice. The first row shows the T2-weighted (b = 0) image together with the mean diffusivity (MD = $\overline{D}$), FA, and MK maps. The second row shows the total neurite water fraction for Examples 1, 2, and 3. The results obtained using both $K_{\max}$ (Ex1a) and $K_{\perp,\max}$ (Ex1b) to estimate f_1 are given with Example 1. For these same four cases, the third row shows the intrinsic intra-neurite diffusivity, and the fourth row shows the extra-neurite mean diffusivity (MDe = $\overline{D}_e$). In Example 1, voxels included in ROI 1 are displayed in color; in Example 2, voxels included in ROI 2 are displayed in color; in Example 3, voxels included in ROI 3 are displayed in color. The maps for Ex1a and Ex1b are nearly identical, demonstrating that choice of whether to use $K_{\max}$ or $K_{\perp,\max}$ to estimate f_1 is of minor practical significance. The intrinsic intra-neurite diffusivity in Example 3 is set a priori to a value of $D^* = 1.0$ μm^2/ms. The other KANDO maps are calculated by minimizing the cost function of Eq. (9). The calibration bars for the diffusivities are in units of μm^2/ms, while the remaining quantities are dimensionless.

Figure 3: Effect of CSF contamination on KANDO estimates of the total neurite water fraction ($1-f_0$), intrinsic intra-neurite diffusivity (D^*), extra-neurite mean diffusivity (MDe = $\overline{D}_e$), as derived from numerical simulations. When CSF volume fraction f_{CSF} vanishes, the plots give the true model parameters. As f_{CSF} increases, the KANDO estimates typically differ from the true values, except for D^* in Example 3, which is assumed to be fixed. For Example 2, Case A corresponds to a fiber crossing angle of 90°, while Case B corresponds to a crossing angle of 75°. For Example 3, Case A corresponds to $f_0 = 1/2$ when $f_{CSF} = 0$, while Case B corresponds to $f_0 = 2/3$ when $f_{CSF} = 0$. The behavior of estimated neurite water fraction is identical for Example 1 and both cases of Example 2; the behavior of D^* is identical for both cases of Example 3. The effect of CSF partial voluming is most pronounced for MDe.

Figure 4: Effect for Example 3 of a difference between the assumed value of the intrinsic intra-neurite diffusivity (D^*) and its true value (D^*_{test}) on KANDO estimates of $1-f_0$, D^*, and MDe, as derived from numerical simulations. The solid circles indicate ideal values for $D^* = D^*_{test}$. Case A corresponds to $f_0 = 1/2$ when $D^* = D^*_{test}$, while Case B corresponds to $f_0 = 2/3$ when $D^* = D^*_{test}$. The plot of D^* vs. D^*_{test} is trivial, as D^* is assumed to be fixed for this KANDO example.

Figure 5: Comparison of parameter estimates for Example 3 as obtained for KANDO and for a direct fit to the signal model of Eq. (42). In all simulations, the assumed intrinsic intra-neurite diffusivity was set to $D^* = 1$ μm^2/ms, while the true value varied from $D^*_{test} = 0$ to 2 μm^2/ms.

Cases A and B are the same as in Fig. 4. The solid circles indicate the ideal values. Estimates derived from the direct fit match the exact values for $D^*_{test} = D^*$. The KANDO predictions, however, have small errors for $D^*_{test} = D^*$, as the KANDO analysis used approximate values for the total diffusivity and kurtosis obtained from the signal, as would be done in a real DKI experiment. (The KANDO predications based on the exact diffusivity and kurtosis are given by Fig. 4.) When $D^*_{test} \neq D^*$, the KANDO and signal model predictions deviate from the ideal values in distinct but qualitatively similar ways.

Table 1

Estimates (with standard deviations) for selected KANDO parameters obtained from in vivo human DKI data.

	ROI 1 Example 1 with $K_{\max}$	ROI 1 Example 1 with $K_{\perp,\max}$	ROI 1 Fieremans model	ROI 1 Example 2	ROI 2 Example 2	ROI 3 Example 3
f_1	0.515 (0.079)	0.512 (0.079)	0.515 (0.079)	0.492 (0.085)	0.357 (0.101)	–
$1-f_0$	"	"	"	0.501 (0.077)	0.405 (0.066)	0.302 (0.068)
D^* [$\mu m^2/ms$]	1.021 (0.281)	1.015 (0.283)	1.174 (0.256)	1.036 (0.314)	0.639 (0.297)	1.0 (assumed)
$\overline{D}_e$ [$\mu m^2/ms$]	1.527 (0.205)	1.520 (0.206)	1.467 (0.193)	1.488 (0.217)	1.358 (0.149)	1.089 (0.324)
$D_{e,\parallel}$ [$\mu m^2/ms$]	2.638 (0.445)	2.633 (0.444)	2.655 (0.420)	2.584 (0.461)	–	–
$D_{e,\perp}$ [$\mu m^2/ms$]	0.971‡ (0.155)	0.965‡ (0.156)	0.874‡ (0.143)	0.940‡ (0.170)	0.891† (0.168)	–

‡Based on average of two smallest eigenvalues of $\mathbf{D}^{(0)}$. †Based on smallest eigenvalue of $\mathbf{D}^{(0)}$.

9. Figure

Click here to download high resolution image

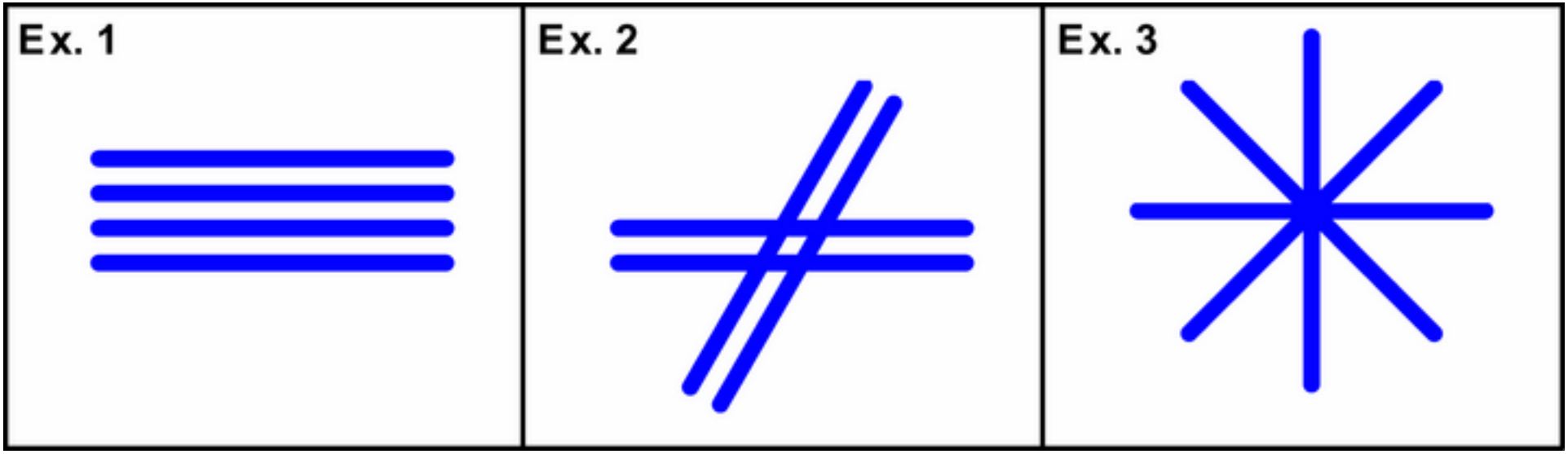

9. Figure

Click here to download high resolution image

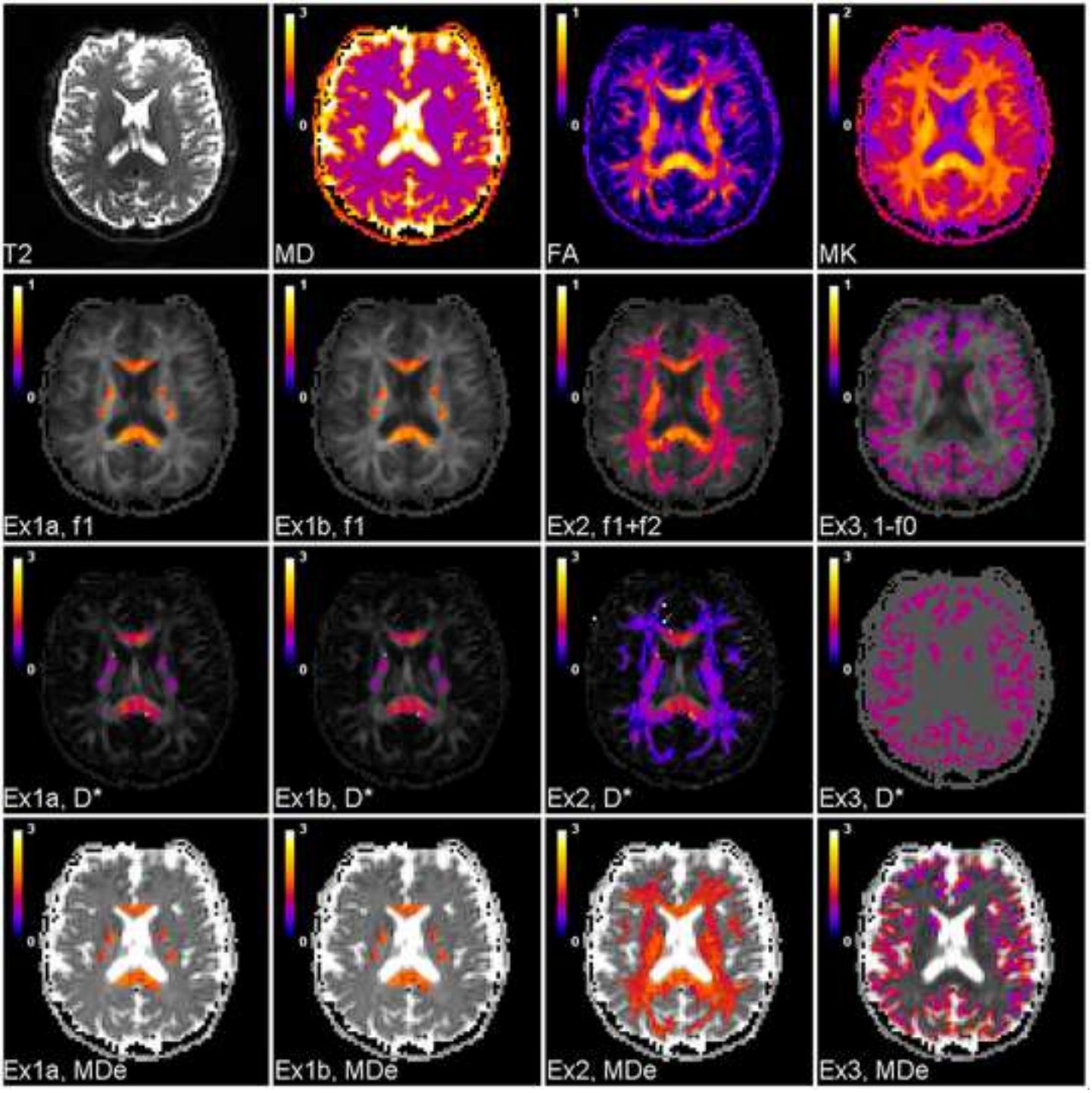

9. Figure

Click here to download high resolution image

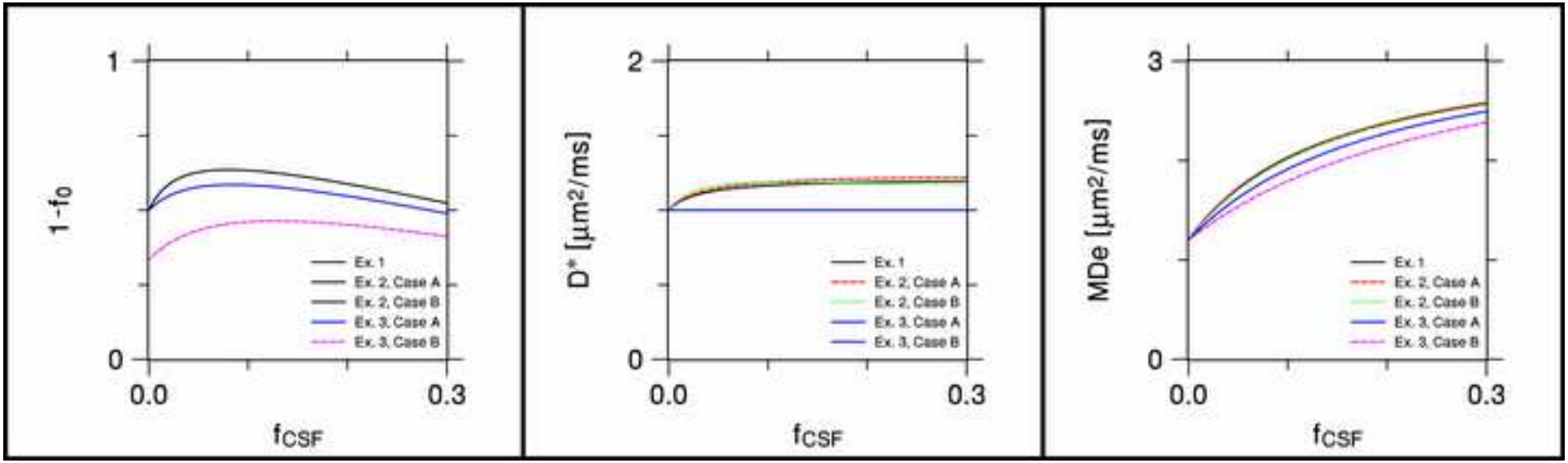

9. Figure

Click here to download high resolution image

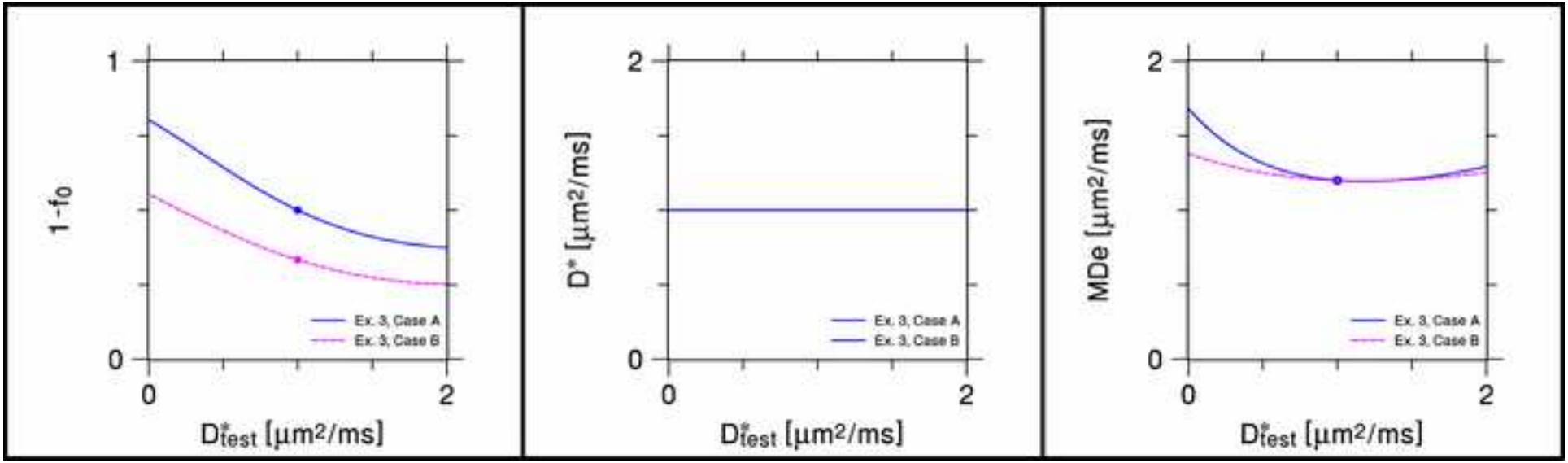

9. Figure

Click here to download high resolution image